

**Bis-tridentate Iridium(III) Phosphors Bearing Functional
2-Phenyl-6-(imidazol-2-ylidene)pyridine and 2-(Pyrazol-3-yl)-6-phenylpyridine
Chelates for Efficient OLEDs**

Jun Lin,^a Nga-Yuen Chau,^{a,b} Jia-Ling Liao,^a Wai-Yeung Wong,^{b,*} Cheng-Yu Lu,^c
Zong-Ting Sie,^c Chih-Hao Chang,^{c,*} Mark A. Fox,^d Paul J. Low,^{e,*} Gene-Hsiang Lee,^f and
Yun Chi,^{a,*}

^a Department of Chemistry, National Tsing Hua University, Hsinchu 30013, Taiwan;
E-mail: ychi@mx.nthu.edu.tw

^b Institute of Molecular Functional Materials, Department of Chemistry and Institute
of Advanced Materials, Hong Kong Baptist University, Waterloo Road, Hong Kong, P. R.
China. E-mail: rwywong@hkbu.edu.hk

^c Department of Photonics Engineering, Yuan Ze University, Chungli 32003, Taiwan;
E-mail: chc@saturn.yzu.edu.tw

^d Department of Chemistry, Durham University, South Road, Durham, DH1 3LE, UK.

^e School of Chemistry and Biochemistry, University of Western Australia, 35 Stirling
Highway, Crawley, 6009, Western Australia, Australia; E-mail: paul.low@uwa.edu.au

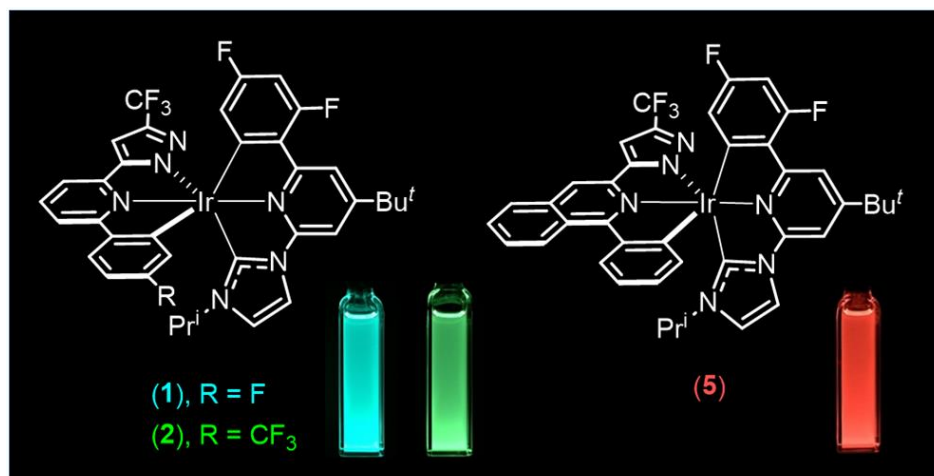
^f Department of Chemistry and Instrumentation Center, National Taiwan University,
Taipei 10617, Taiwan

Abstract

Pro-ligands to the monoanionic tridentate chelate 4-(*t*-butyl)-2-(2,4-difluorophenyl)-6-(3-isopropyl-imidazol-2-ylidene)pyridine (phpyim-H₂)PF₆, and dianionic tridentate chelates derived from functional 2-pyrazol-3-yl-6-phenylpyridine chelates, i.e. L1-H₂ – L5-H₂, have been synthesized and characterized. Treatment of (phpyim-H₂)PF₆ with [Ir(COD)(μ-Cl)]₂ in the presence of sodium acetate, followed by heating at 200 °C with one eq. of the dianionic

chelate, afforded the respective charge-neutral, *bis*-tridentate Ir(III) complexes [Ir(phpyim)(L1)] (**1**) – [Ir(phpyim)(L5)] (**5**). A hydride complex [Ir(phpyim)(L5-H)(H)] (**6**) was made when the ‘one-pot’ reaction of (phpyim-H₂)PF₆, [Ir(COD)(μ-Cl)]₂ and L5-H₂ was carried out at 140 °C. Complex **6** is likely an intermediate in the formation of **5** as it is converted to **5** on heating to 200 °C. Compounds **1** – **6** have been characterized by NMR spectroscopy and, in the cases of **1**, **5** and **6**, by X-ray structural analysis. TD-DFT computations confirmed that the emission bands are derived from ³MLCT transitions involving the chelates L1–L5, resulting in a wide range of emission wavelengths from 473 (cyan) to 608 (orange-red) nm observed for **1** – **5**. A series of green- and red-emitting organic light-emitting diodes (OLEDs) with a simplified tri-layer architecture were fabricated using the as-prepared Ir(III) complexes **2** and **5**, respectively. A maximum external quantum efficiency of 18.8%, a luminance efficiency of 58.5 cd/A, and a power efficiency of 57.4 lm/W were obtained for the green-emitting OLEDs (**2**), which compares with 15.4%, 10.4 cd/A, and 9.0 lm/W obtained for the red-emitting OLEDs (**5**). The high efficiencies of these OLED devices suggest great potential for these *bis*-tridentate Ir(III) metal phosphors in the fabrication of multicolor OLED devices.

TOC illustration



Cyan- to red-emitting Ir(III) metal complexes comprising the *bis*-tridentate architecture, i.e. with both 2-(2,4-difluorophenyl)-6-(3-isopropyl-imidazol-2-ylidene)pyridine and functional 2-pyrazol-3-yl-6-phenylpyridine, were found to be useful for the fabrication of efficient OLEDs.

Introduction

Since the first report on organic electroluminescence (EL) in 1987,¹ there has been continued interest in the development of organic light-emitting diodes (OLEDs) for use in the next generation of display and lighting technologies. Over the past two decades, phosphors based on third-row, late transition-metal complexes have emerged as compelling molecules in these areas of research, offering high luminescent efficiencies. Whilst organic emitters are best described as fluorescent materials, which emit only through singlet excitons (i.e. only 25% of the total excitons), the efficient singlet/triplet intersystem crossing induced by the third-row transition-metal elements allows efficient harvesting of both the singlet and triplet excitons generated during electrical excitation, which, in the ultimate limit, can give rise to an unitary internal quantum efficiency.² In this regard, Os(II), Ir(III) and Pt(II) complexes have attracted much attention because of their great potential to exhibit both greater emission efficiency and color tunability through control and optimization of the supporting ligand spheres.³

To date, most of the Ir(III) phosphors bear three bidentate chelates such as cyclometalated 2-phenylpyridine (ppy) in the prototypical example $[\text{Ir}(\text{ppy})_3]$.⁴ However, Williams and Haga have independently reported a class of Ir(III) complexes with formula $[\text{Ir}(\text{dpyx})(\text{ppy})\text{Cl}]$, dpyxH = 4,6-dipyridylxylene, using both bidentate and tridentate cyclometalating ligands.⁵ In contrast, studies on the *bis*-tridentate Ir(III) complexes, have met only with limited success,⁶ among which $[\text{Ir}(\text{dpyx})(\text{dppy})]$ (dppy = 2,6-diphenylpyridine) and $[\text{Ir}(\text{fpbpy})(\text{dppy})]$ (fpbpy = 6-(5-trifluoromethylpyrazol-3-yl)-2,2'-bipyridine) provided the basic model, i.e. the need for a pair of monoanionic and dianionic chelates in assembling the charge-neutral *bis*-tridentate architecture (Chart 1).⁷ Recently, we also discovered that theazole-containing dianionic chelate such as 2-(pyrazol-3-yl)-6-phenylpyridine can be employed in the preparation of the relevant *bis*-tridentate Ir(III) complexes with tunable color and enhanced efficiencies that are desirable for OLED applications.⁸

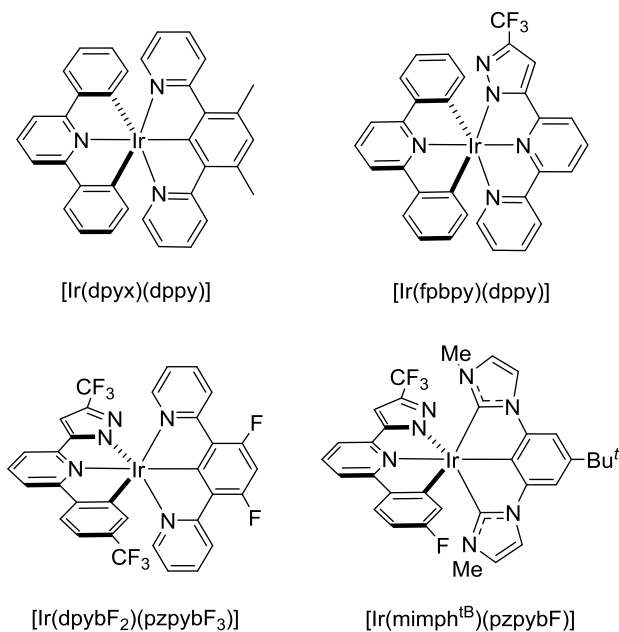


Chart 1: Ir(III) complexes featuring two distinctive tridentate chelates.

However, due to the enhanced stabilization effect exhibited by tridentate ligands, these complexes are expected to be even more kinetically stable than the traditional *tris*-bidentate counterparts. Therefore, *bis*-tridentate complexes offer the possibility of further improved chemical stability and resistance against cleavage of metal-ligand bonds upon chemical or electrical excitations, as well as increased structural rigidity, which may subdue the undesirable non-radiative decay processes. These expectations motivate us to investigate the generalized design and routes that could afford the *bis*-tridentate Ir(III) complexes, and further explore their potential for use as phosphors for efficient OLED applications.⁹

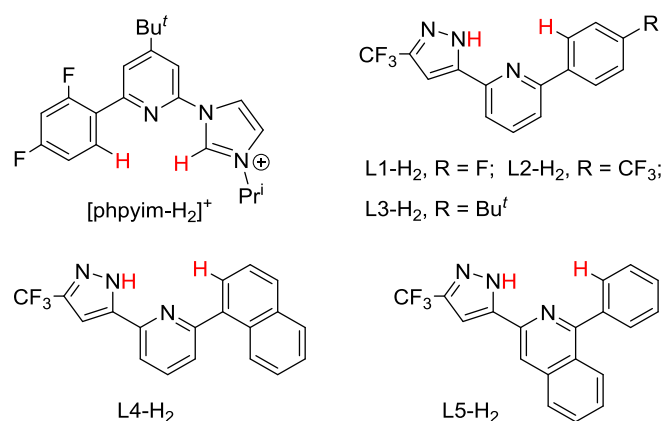


Chart 2: The tridentate chelate precursors employed in this study.

Bearing this in mind, we have prepared charge-neutral Ir(III) phosphors using the monoanionic tridentate chelate phpyim i.e. 4-(*t*-butyl)-2-(2,4-difluorophenyl)-6-(3-isopropyl-imidazol-2-ylidene)pyridine, from [phpyim-H₂]⁺ salts, and various dianionic tridentate chelates with the 2-pyrazol-3-yl-6-phenylpyridine core skeleton, from their precursors i.e. 2-(5-trifluoromethyl-1H-pyrazol-3-yl)-6-(4-fluorophenyl)pyridine (L1-H₂), 2-(5-trifluoromethyl-1H-pyrazol-3-yl)-6-(4-trifluoromethylphenyl)pyridine (L2-H₂), 2-(5-trifluoromethyl-1H-pyrazol-3-yl)-6-(4-*t*-butylphenyl)pyridine (L3-H₂), 2-(5-trifluoromethyl-1H-pyrazol-3-yl)-6-naphthylpyridine (L4-H₂) and 1-phenyl-3-(5-trifluoromethyl-1H-pyrazol-3-yl)isoquinoline (L5-H₂) showed in Chart 2. As similar dianionic tridentate chelates are known to form stable complexes with the isoelectronic Ru(II) and Os(II) metal atoms,¹⁰ we anticipated that these ligands are equally suitable for the synthesis of the respective charge-neutral, *bis*-tridentate Ir(III) phosphors. Indeed, the successful coordination of both phpyim and dianionic chelates L1 – L5 around the Ir(III) metal center have led to the isolation of *bis*-tridentate Ir(III) complexes [Ir(phpyim)(Ln)] n = 1 ~ 5, (**1** ~ **5**) with the observed emission color ranging from cyan (**1**) to orange-red (**5**). By lowering the reaction temperature with the isoquinolinyl pro-chelate ligand L5-H₂, a metal-hydride complex [Ir(phpyim)(L5-H)H] (**6**) was isolated. Complex **6** has the L5-H chelate in a bidentate bonding mode, where the pyrazolyl ligand sits *trans* to the pyridine donor in phpyim, and the hydride located opposite to the isoquinolinyl fragment. Chart 3 depicted the structural drawings of these synthesized Ir(III) metal phosphors and intermediate. A series of OLEDs were fabricated using phosphors **2** and **5** which has laid a solid foundation for further exploration of *bis*-tridentate Ir(III) metal complexes as efficient OLED emitters.

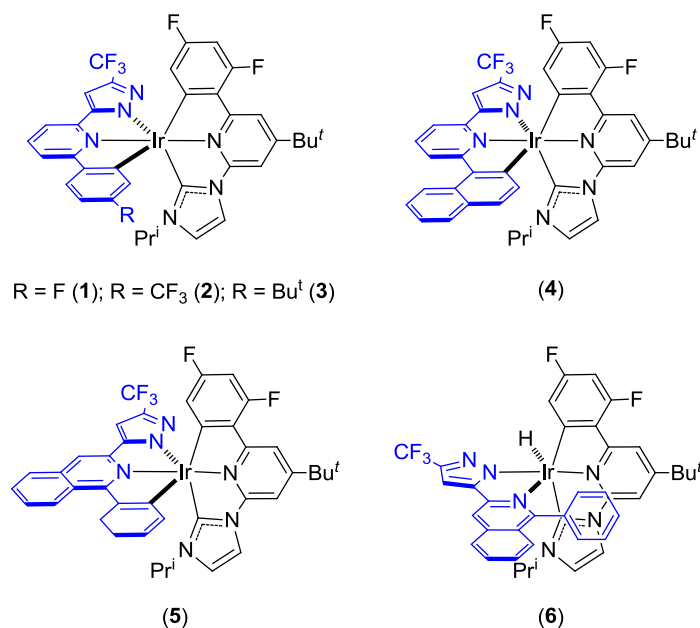
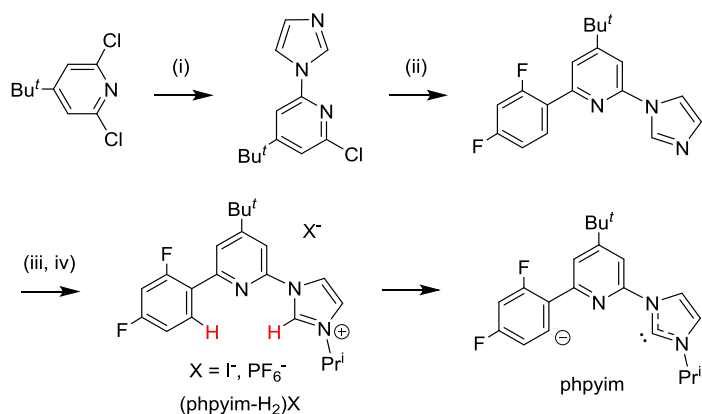


Chart 3: The *bis*-tridentate Ir(III) complexes discussed in this study.

Results and Discussion

Synthesis and structural characterization. The precursor to the monoanionic tridentate chelate 4-(*t*-butyl)-2-(2,4-difluorophenyl)-6-(3-isopropyl-imidazol-2-ylidene)pyridine (phpyim-H₂)PF₆, was synthesized using a multi-step protocol (Scheme 1). First, treatment of 4-(*t*-butyl)-2,6-dichloropyridine and imidazole in the presence of tetrabutylammonium bromide (NBu₄Br) as a phase transfer catalyst afforded the pyridine-imidazole derivative. This imidazole derivative was then reacted with 2,4-difluorophenylboronic acid in the presence of catalytic Pd(dppf)Cl₂ to form 4-(*t*-butyl)-2-(2,4-difluorophenyl)-6-(1*H*-imidazol-1-yl)pyridine. Subsequently, the isolated phenyl-pyridine-imidazole derivative was treated with 2-iodopropane in toluene solution to afford 1-[4-(*t*-butyl)-6-(2,4-difluorophenyl)pyridin-2-yl]-3-isopropyl-1*H*-imidazol-3-ium iodide (phpyim-H₂)I. Anion exchange with NH₄PF₆ resulted in the precipitation of the corresponding PF₆ salt, (phpyim-H₂)PF₆. This pro-ligand forms the monoanionic tridentate ligand phpyim in the presence of sodium acetate, which is basic enough to

induce the imidazolium to imidazol-2-ylidene conversion.



Scheme 1. (i) imidazole, KOH, NBu₄Br, 80 °C; (ii) Pd(dppf)Cl₂, F₂H₃C₆B(OH)₂, toluene/ethanol/H₂O, 110 °C; (iii) PrⁱLi, toluene, 80 °C; (iv) NH₄PF₆, H₂O/ethanol, RT.

Preparation of the corresponding *bis*-tridentate Ir(III) metal complexes was typically executed in a two-step process. Firstly, the imidazolium ligand (phpyim-H₂)PF₆ was treated with [Ir(COD)(μ-Cl)]₂ in the presence of sodium acetate in refluxing acetonitrile. We expected that sodium acetate is capable of inducing both the cyclometalation of phenyl group and formation of imidazol-2-ylidene moiety at the same time, affording an Ir(III) intermediate bearing the tridentate phpyim chelate. Without isolation and characterization of the intermediate species, acetonitrile was replaced by decalin as the solvent, together with the addition of a second tridentate ligand, Ln-H₂, n = 1 – 5. The resulting mixture was then brought to reflux overnight at 200 °C. The cyan- to red-emitting Ir(III) metal complexes [Ir(phpyim)(Ln)], (**1–5**), were isolated by silica gel column chromatography, followed by recrystallization. The isoquinolinyl pro-chelate L5-H₂ gave [Ir(phpyim)(L5-H)H] (**6**) containing the bidentate L5-H chelate and retention of a metal-hydride fragment instead of complex **5** if the ‘one-pot’ reaction was conducted in refluxing xylene at 140 °C. As expected, the bidentate L5-H chelate in **6** underwent phenyl C-H activation to form the thermodynamic product [Ir(phpyim)(L5)] (**5**) upon heating in decalin at 200 °C. Hence, the complex with a bidentate Ln-H chelate plus a hydride around the coordination

sphere may be an intermediate to the formation of every *bis*-tridentate product made here.

Single crystal X-ray diffraction studies of the Ir(III) complexes **1** and **5** confirm the co-existence of two tridentate chelates arranged in the orthogonal, *bis*-tridentate bonding mode (Figures 1 and 2). The monoanionic phpyim chelate of both complexes exhibits short Ir-C distances for the terminal phenyl and carbene fragments (c.f. Ir-C(1) = 2.040(4) and Ir-C(12) = 2.047(5) Å for **1**; Ir-C(33) = 2.037(4) and Ir-C(20) = 2.051(3) Å for **5**), which are consistent with the respective Ir-C distances observed in Ir(III) complexes bearing both central cyclometalating entity and *trans*-disposed NHC carbene unit.¹¹ On the other hand, the phenyl fragment of the dianionic pyrazol-3-yl phenylpyridine chelates L1 and L5 shows an even shorter Ir-C distance (Ir-C(22) = 2.024 (5) Å for **1**; Ir-C(1) = 2.016(3) Å for **5**), located *trans* to the anionic pyrazolate fragment, which in turn contains long Ir-N bond lengths (Ir-N(4) = 2.113(4) Å for **1**; Ir-N(2) = 2.097(3) Å for **5**). In sharp contrast, the Ir-N distance of the central pyridyl fragment in both tridentate chelates L1 or L5 (Ir-N(1) = 1.990(4) and Ir-N(4) = 1.995(4) Å for **1**; Ir-N(1) = 1.999(3) and Ir-N(6) = 1.996(3) Å for **5**) are notably shorter than all other metal-ligand distances of the peripheral donors, which is attributed to the inherent geometrical constraint imposed. Shortening of the metal-ligand distance at the central ligating unit, versus those at the peripheral donors, has been well documented in metal complexes with terpyridine and other functional tridentate chelates.^{10c}

The X-ray analysis of **6** showed two crystallographically independent, but structurally similar molecules within the crystal lattices, for which only one is depicted in Figure 3. Like in **1** and **5**, the tridentate phpyim chelate has the phenyl and imidazolylidene Ir-C distances of 2.051(3) and 2.027(3) Å and a contracted Ir-N distance of 1.996(2) Å. However, the L5-H ligand is now coordinated to the Ir(III) atom with pyrazolate located *trans* to the central pyridine unit of phpyim. As a result, the phenyl group of L5-H resides opposite to the hydride and adopts a twisted orientation versus the chelate to reduce steric interaction with the phpyim chelate.

This molecular structure is reminiscent to that of the recently reported Ir(III) intermediate with the phenyl dicarbene and similar dianionic chelates.^{8b}

Photophysical data. The UV-Vis absorption and emission spectra of **1–5** were recorded at room temperature (RT) in CH₂Cl₂ solution (Figure 3 and Table 1). All complexes **1–5** show very strong absorption bands below 350 nm ($\epsilon > 1.4 \times 10^4 \text{ M}^{-1}\cdot\text{cm}^{-1}$) due to ¹ $\pi\pi^*$ transitions localized on both the tridentate chelates, together with a set of less intense bands in the region $> 400 \text{ nm}$ ($\epsilon > 3 \times 10^3 \text{ M}^{-1}\cdot\text{cm}^{-1}$), which are attributed to MLCT transitions from the Ir(III) metal ion to the tridentate chelates. For the Ir(III) complexes **1**, **2** and **3**, the lowest energy ¹MLCT absorption maximum is at $\sim 410 \text{ nm}$, involving the common pyrazol-3-yl phenylpyridine core (i.e. Ln) such as L1–L3 and the monoanionic phpyim ligand. Introduction of the naphthyl moiety (L4) or replacement of the central pyridyl group with isoquinolinyl fragment (iq of L5), forming **4** and **5**, gives significantly red-shifted ¹MLCT absorptions at 458 and 481 nm, respectively. The spin-forbidden ³MLCT absorptions along with the ³ $\pi\pi^*$ transitions were not observed due to the lowered extinction coefficient.

Figure 4 also depicts the emission spectra of **1–5**, showing the influence imposed by the Ln substituents in L1–L3, and the effect of increased π -conjugation of L4 and L5 chelates. As can be seen in Figure 3, the Ir(III) complexes **1–3** showed relatively blue-shifted emissions. The vibronic fine structures implies notable contributions from ligand-centered $\pi\pi^*$ transitions. Replacing the fluoro substituent of L1 in **1** with CF₃ in **2** and *t*-butyl group in **3** red-shifts the highest energy peak maximum from 473 to 495 and 481 nm respectively.

The naphthyl moiety in place of the peripheral phenyl group of L1 shifts the emission peak wavelength to 583 nm in **4** compared to 473 nm in **1** with a large energy difference of 0.5 eV. The emission profile for **4** is much less structured than for the other complexes, **1–3** and **5**. This is unexpected as DFT calculations predict the dominant ligand-centered $\pi\pi^*$ transitions in **4** which should lead to a structured emission profile. Replacement of the central pyridyl unit with isoquinolinyl group in L5 shifts the emission peak wavelength to 608 nm for **5**. The extended π -conjugation

units present in the L4 and L5 chelates decrease the $\pi\pi^*$ transition energies leading to red-shifted emissions.

In Table 1, emission quantum yields (Q.Y.) of nearly 100% were observed for the Ir(III) complexes **1–3**, with the parent Ln chelate such as L1, L2 and L3. Apparently, the *bis*-tridentate architecture in these Ir(III) complexes increases the radiative decay and reduces the non-radiative decay processes and, hence, improves their Q.Y.s.

The observed lifetimes for complexes **1–5** are intriguing as well, and the lifetimes would decrease with increasing Q.Y.s. The shortest lifetime is 3.01 μs for **3** with the highest Q.Y. whereas the longest lifetime is 9.23 μs for **4** with the lowest Q.Y. Complex **4** may contain a different photophysical process as the peak profile for **4** is less structured. Accordingly, the naphthyl group has a detrimental effect on the solution luminescence compared to the phenyl group it replaces.

The reduced Q.Y.s could also be partially offset by the higher rigidity of chelate in **5** vs **4**, as the central isoquinoliny fragment L5 in **5** is buttressed by two peripheral substituents, for which the total stiffness could be greater than the chelate L4 with a terminal naphthyl appendage in **4**. The radiative rate constant of **5** ($k_r = 1.1 \times 10^5 \text{ s}^{-1}$), calculated from equations:

$$(k_r + k_{nr}) = 1 / \tau_{\text{obs}}$$

and

$$\text{Q.Y. (\%)} = k_r / (k_r + k_{nr}),$$

is notably larger than that of **4** ($k_r = 2.7 \times 10^4 \text{ s}^{-1}$), while both complexes exhibit similar magnitude of non-radiative rate constants ($k_{nr} = 7.5 \times 10^4 \text{ s}^{-1}$ for **5** and $k_{nr} = 8.1 \times 10^4 \text{ s}^{-1}$ for **4**). This implies that the ligating motif in **5** is critical to the enhanced radiative process (i.e. as shown by the increased k_r), but not so much to the non-radiative decay (i.e. identical k_{nr}) versus the naphthyl substituted Ir(III) complex **4**.

Electrochemistry. The electrochemical behavior of these Ir(III) complexes was measured, for which the corresponding redox data are listed in Table 2. Each of the complexes **1–5** showed a reversible metal-centered oxidation peak potential ($E^{\text{Ox}}_{1/2}$) in

the region of 0.54 ~ 0.71 V and an irreversible reduction peak potential (E_{pc}^{Re}) between -2.40 ~ -2.67 V, respectively. For the first three complexes **1–3**, the trend of the oxidation potentials is consistent with the presence of electron-withdrawing substituents on the tridentate Ln chelates (i.e. L1 and L2) that shifts the potentials to the more positive direction, i.e. **2** (0.71 V) > **1** (0.66 V) > **3** (0.57 V) with CF₃, fluorine and *t*-butyl substituent, respectively. The peak potential of 0.54 V for **4** suggests that the naphthyl group is involved in the HOMO, presumably via π -conjugation thus resulting in a more negative oxidation potential. On the other hand, the oxidation potential of **5** (0.57 V) is similar to **3**, indicating that the isoquinolinyl substituent has little effect on the HOMO. While the reduction waves are irreversible, the less negative reduction potential of -2.40 V observed for **5** by at least 0.18 V compared to that of **1 – 4** (-2.58 to -2.67 V) implies that the LUMO is mainly located on the isoquinolinyl moiety in **5**.

DFT calculations. To investigate the optoelectronic properties of complexes **1–5**, calculations based on density functional theory (DFT) and time-dependent density functional theory (TD-DFT) were undertaken. The B3LYP hybrid DFT functional with a LANL2DZ basis set on iridium atom and 6-31G** on all other atoms, as well as a conductor-like polarization continuum (CPCM) model in the CH₂Cl₂ solvent were employed. The results of the geometry data after optimization for the Ir(III) complexes **1–5** are summarized in Table S1. The majority of bond lengths are over-estimated by only ca. 0.03 Å compared with the crystallographically determined structures, with a slightly larger difference in the case on the Ir-N bonds associated with the anionic pyrazolyl moiety (ca. 0.05–0.06 Å). Nevertheless, agreement between the experimental and calculated structures gives high confidence in the accuracy of the optimized geometries.

Plots of the HOMO, LUMO and LUMO+1 for complexes **1–5** are given in Figure 5 and the percentages of orbital contributions from each designated group in **1–5** are listed in Tables S2–S6. The HOMOs of **1–3** contain significant contributions from the Ir(III) d_{π} orbitals (Ir, 31 ~ 34%) admixed with contributions from the phenyl fragment

of the pyrazolyl Ln chelates. The metal contribution in the HOMO decreases in **5** (Ir, 26%) and even further in **4** (Ir, 22%). It is worth noting that there may be a relationship between the Q.Y.s and the iridium metal contributions in the HOMOs where the decreasing trend in Q.Y.s of **1–3** (91–100%), **5** (57%) and **4** (25%) parallel the decreasing iridium d_{π} contributions in the HOMO of these complexes.

The discussion of the LUMO and LUMO+1 in each complex is necessary as there are two distinct pyridyl moieties in the phpyim and L1–L4 chelates where the LUMO and LUMO+1 can be close in energy (Table 2). The relative ordering of these LUMOs, i.e. pyridyl (or isoquinoliny) π^* systems, varies along the series, (**1**: LUMO = phpyim-py, LUMO+1 = L1-py; **2**: LUMO = L2-py, LUMO+1 = phpyim-py; **3**: LUMO = phpyim-py, LUMO+1 = L3-py; **4**: LUMO = L4-py, LUMO+1 = phpyim-py; **5**: LUMO = L5-iq, LUMO+1 = phpyim-py) with the CF_3 group in L2 and naphthyl and isoquinoliny groups in L4 and L5 bringing the corresponding orbitals lower in energy than the respective phpyim chelate. TD-DFT computations (*vide infra*), however, predict that the observed emissions in this study involve the pyridyl (or isoquinoliny) unit at the Ln chelate in all cases.

The significantly longer emission wavelengths in **4** and **5** compared to those for **1–3** are due to the considerably smaller HOMO-LUMO energy gaps in **4** and **5** by different factors. In **4**, the HOMO energy is raised by the naphthyl group whereas, in **5** with an even longer emission wavelength, the LUMO energy is considerably lowered by the isoquinolyl unit.

In considering the optical absorption and emission properties of **1–5**, it is clear that the studied Ir(III) complexes can be considered as belonging to three distinct groups, **1–3**, **4** and **5**. The general order of the $^1\text{MLCT}$ bands observed in the experimental spectra (Figure 4) is adequately reproduced by the results of TD-DFT calculations. (**1**: $S_0 \rightarrow S_1$ 406 nm, ML(phpyim)-CT and $S_0 \rightarrow S_2$ 387 nm, ML(L1)-CT; **2**: 404 and 401 nm; **3**: 413 and 393 nm). In agreement with experiment, the $^1\text{MLCT}$ transitions in **4** (423 and 420 nm) and **5** (454 and 419 nm) are red-shifted in comparison with those of **1–3**.

The triplet energies (albeit with zero oscillator strength in these computational models which ignore spin-orbit coupling) on the optimized ground state geometries were calculated to give some insight into the nature of the emission in these Ir(III) complexes **1–5**. It is assumed here that the nature of the emission mirrors the absorption data obtained from the optimized S_0 ground state geometries. The TD-DFT calculated $S_0 \rightarrow T_n$ transition energies do not take into account the Stokes shifts expected from $S_0 \leftarrow T_n$ transitions, and hence the predicted emission energies would be over-estimated.¹² Hence, the predicted absorption energies are converted by assuming a Stokes shift energy scaling factor for predicted emission energies which are in excellent agreement with the observed emission maxima (Table 1). The $S_0 \leftarrow T_1$ transition is rather well described as $^3MLn(py)$ -CT in **1–4**, or $^3ML5(iq)$ -CT in the case of **5**. Interestingly, they are not $^3M(phpyim)$ -CT as might have been expected for complexes **1** and **3** based on their LUMOs from DFT calculations. In accord with the measured absorption spectra and CV traces, the tuning of the emission color is largely due to changes in the tridentate Ln chelates.

OLED Device Fabrication. Complexes **2** and **5** were selected as dopants to investigate applications in electroluminescent (EL) devices because of their higher photoluminescence (PL) Q.Y. as well as their saturated green and red emission colors. In this study, optimization of the device architecture was achieved following a sequence of (i) selecting a suitable host material for the emission layer (EML), (ii) choosing an appropriate hole-transport layer (HTL) and electron-transport layer (ETL), (iii) adjusting the thickness of the HTL, and (iv) varying the dopant concentration. Considering the triplet energy gaps (E_T) of **2** and **5**, the host materials should possess triplet energy gaps higher than 2.7 eV to ensure sufficient energy transfer as well as exciton confinement. In addition, hosts with bipolar transport capability allow for the convenient adjustment of carrier recombination and carrier balance. Four potential hosts including 4,4'-N,N'-dicarbazolebiphenyl (CBP), 3-bis(9-carbazolyl)benzene (mCP), 2,6-bis(3-(9H-carbazol-9-yl)phenyl)pyridine (26DCzppy), 2,6-di(9H-carbazol-9-yl) pyridine (PYD-2Cz) were tested.¹³ Furthermore,

1,1-bis[(di-4-tolylamino)phenyl]cyclohexane (TAPC) and 1,3,5-tri[(3-pyridyl)-phen-3-yl]benzene (TmPyPB) were respectively selected as the HTL and ETL of OLEDs with green-emitting complex **2**, because their wide triplet energy gaps (about 2.87 and 2.78 eV, respectively) promote high energy exciton confinement.¹⁴ The mCP-based device exhibited a higher external quantum efficiency (EQE) of 16.6%, versus devices using other host materials (c.f. 12.9% for PYD-2Cz; 14.0% for 26DCzppy; 15.2% for CBP). On the other hand, the same bipolar hosts were also used to examine the host-guest system in OLEDs for complex **5**. In general, a certain degree of hole trapping phenomenon caused by the narrower gap of the dopant could be compensated by adopting an ETL with lower mobility. Therefore, compared to TmPyPB with a higher electron mobility of $\sim 10^{-3}$ cm²/Vs, 3,5,3',5'-tetra(*m*-pyrid-3-yl)-phenyl[1,1']biphenyl (BP4mPy) with adequate electron mobility (i.e. $\sim 10^{-4}$ cm²/Vs) is more suitable for use as the ETL in red-emitting OLEDs.¹⁴ Experimental results showed that superior carrier balance was obtained by using the CBP host. The respective maximum EQE of OLEDs with CBP, mCP, 26DCzppy, and PYD-2Cz hosts were evaluated to be 10.7%, 9.7%, 10.6%, and 9.8%. Thus, mCP and CBP were respectively chosen as the host materials for complexes **2** and **5** based on the outcomes of host-guest tests.

Because of the mismatched refractive indices of the ITO and organic layers, the thicknesses of ITO and HTL would also affect the out-coupling efficiency.¹⁵ Based on our previous experience, the thicknesses of ITO for green and red phosphorescent OLEDs were set at 70 nm and 90 nm, respectively. In addition, the hole mobility of TAPC was reported to be 10^{-2} cm²/Vs, allowing us to alter the thickness of HTL without significantly increasing the operation voltage.^{14a,b} Thus, OLEDs were designed with variable TAPC thickness to examine the effect of out-coupling.¹⁶ The green OLEDs were fabricated with a simplified tri-layer architecture consisting of ITO (70 nm)/ TAPC (*x* nm)/ mCP with 4 wt.% **2** (20 nm)/TmPyPB (50 nm)/ LiF (0.8 nm)/ Al (150 nm), while the architecture of the red OLEDs was set to ITO (90 nm)/ TAPC (*y* nm)/ CBP with 4 wt.% **5** (20 nm)/ BP4mPy (40 nm)/ LiF (0.8 nm)/ Al (150 nm), where

LiF and aluminum respectively served as the electron injection layer and reflective cathode. The x and y were varied from 40 nm to 70 nm (cf. Figure S7). The results indicate that the optimal thickness of TAPC was 70 nm and 40 nm for green and red OLEDs, respectively. Figure 6 presents the structures of the employed materials along with the schematic architecture of the as-fabricated OLEDs.

The EL spectra of the above mentioned OLEDs are shown in Figure 7(a). All OLEDs showed EL spectra similar to the respective PL spectra of **2** and **5**, confirming the effective energy transfer between the host and guest as well as the carrier recombination well within the EML.¹⁷ Hence, the installed HTL and the ETL have provided good confinement and avoided the exciton diffusion to the adjacent layers.¹⁸ The slight variation in EL in both devices is mainly due to the different optical interference.¹⁹ Moreover, the corresponding green and red devices showed stable CIE coordinates of (0.27, 0.60) and (0.67, 0.33) within a wide range of luminance from 10^2 to 10^4 cd/m², respectively. It is worth mentioning that the CIE coordinates of device R doped with 4 wt.% of **5** superimpose to the deep-red apex of NTSC.

Figure 7(b) shows the current density-voltage-luminance (J - V - L) curves of the tested devices. As expected, an increase in the HTL thickness in devices G and R led to lowered current densities. Compared to the J - V curves of both series of devices G and R, the higher current densities in device R resulted from the use of a thinner ETL as well as the 90 nm-ITO with a lower sheet resistance. Figures 7(c) and (d) show the trend for efficiency versus luminescence. Clearly, the efficiency of devices G increased with the TAPC thickness, while the efficiency of devices R stayed essentially unchanged. Based on these findings, the optimized TAPC thickness was set as 70 nm and 40 nm for the devices G and R, respectively. This architecture was further optimized using 2 and 8 wt.% of dopants. The EL characteristics as well as the corresponding numerical data of the tested devices are depicted in Figure 7 and Table 3.

Figure 7(a) shows the EL spectra of both devices G and R with different doping

concentrations where no other emission except for that of dopant was observed even at the low concentration of 2 wt.%, implying effective energy transfer in these host-guest systems. From the *J-V-L* curves shown in Figure 7(b), the current densities of both devices reached the highest values at a doping level of 4 wt.%. In general, the carrier transport capability of dopant is affected by both the energy level and doping concentration,²⁰ and the latter also influences the site of carrier recombination.²¹ Thus, the maxima obtained at 4 wt.% might be the result of fine balance between carrier trapping and transport. The lowest turn-on voltages (i.e. 3.3 V and 4.0 V) of both devices were also recorded at this doping concentration. As shown in Figures 7(c) and (d), the corresponding maximum efficiencies of devices G and R reached 18.8% (58.5 cd/A, and 57.4 lm/W) and 12.5% (10.4 cd/A and 9.0 lm/W). Hence, these devices were calculated to possess nearly 100% of internal quantum efficiency based on their observed EL and PL efficiencies.²² Furthermore, devices G and R at 4 wt.% of **2** and **5** maintain forward efficiencies of 15.3 % (47.6 cd/A, and 31.0 lm/W) and 11.1 % (9.3 cd/A, and 4.7 lm/W) at 10^2 cd/m², respectively. Overall, these recorded performances demonstrated the high potential of these bis-tridentate Ir(III) complexes in OLED applications.

Conclusions

In summary, a new series of Ir(III) based phosphors with *bis*-tridentate chelating architecture were synthesized and characterized. Of particular interest is the design of the monoanionic tridentate chelate, i.e. phpyim: 4-(*t*-butyl)-2-(2,4-difluorophenyl)-6-(3-isopropyl-imidazol-2-ylidene)pyridine, and the dianionic tridentate Ln chelates bearing a 2-pyrazol-3-yl-6-phenylpyridine based design, i.e. L1–L5. With these ligands, our studies showcase a rare example of tridentate chelates that are capable of coordinating to an Ir(III) atom to give a *bis*-tridentate charge-neutral assembly. TD-DFT calculations indicate emissions to largely originate from ³MLnCT processes, together with contribution from ligand-centered $\pi\pi^*$ transition, and the emission color is heavily influenced by the

dianionic chelate Ln with the maxima ranging from 473 to 608 nm. OLED devices fabricated using simplified tri-layer architecture and phosphors **2** and **5** demonstrated high performance. The green OLEDs using **2** gave a peak external quantum efficiency of 18.8%, a luminance efficiency of 58.5 cd/A, and a power efficiency of 57.4 lm/W, while the device with **5** showed maximum efficiencies of 12.5 %, 10.4 cd/A, and 9.0 lm/W. Moreover, the device with complex **5** exhibits a saturated red emission and the CIE coordinates superimpose to the deep-red apex of NTSC, which fulfills the requirements for high color saturation in display applications.

Experimental section:

General Information and Materials. All reactions were performed under a nitrogen atmosphere and solvents were distilled from appropriate drying agents prior to use. Commercially available reagents were used without further purification unless otherwise stated. 4-(*t*-Butyl)-2,6-dichloropyridine was prepared by a consecutive double chlorination of 4-*t*-butylpyridine.²³ The dianionic tridentate chelates with 2-pyrazol-3-yl-6-phenylpyridine class of core skeleton, i.e. 2-(5-trifluoromethyl-1*H*-pyrazol-3-yl)-6-(4-fluorophenyl)pyridine (L1-H₂), 2-(5-trifluoromethyl-1*H*-pyrazol-3-yl)-6-(4-trifluoromethylphenyl)pyridine (L2-H₂), 2-(5-trifluoromethyl-1*H*-pyrazol-3-yl)-6-(4-*t*-butylphenyl)pyridine (L3-H₂), 2-(5-trifluoromethyl-1*H*-pyrazol-3-yl)-6-naphthylpyridine (L4-H₂) and 1-phenyl-3-(5-trifluoromethyl-1*H*-pyrazol-3-yl)isoquinoline (L5-H₂) were prepared using the reported method, followed by hydrazine cyclization.²⁴ ¹H, ¹³C and ¹⁹F NMR spectra were measured with a Varian Mercury-400 or Bruker Avance 500 instrument. Mass spectra were recorded on a JEOL SX-102A instrument operating in electron impact (EI) or fast atom bombardment (FAB) mode. The elemental analysis was carried out on a Heraeus CHN-O Rapid Elementary Analyzer. UV-Vis spectra were recorded on a HITACHI U-3900 spectrophotometer. Steady-state emission spectra and lifetimes were measured according to those described in the literature.²⁵

1-(4-(*t*-Butyl)-6-(2,4-difluorophenyl)pyridin-2-yl)-3-isopropyl-1*H*-imidazol-3-ium

hexafluorophosphate, (phpyim-H₂)PF₆

A mixture of 4-(*t*-butyl)-2,6-dichloropyridine (1.3 g, 6.37 mmol), imidazole (0.48 g, 7.01 mmol) and potassium hydroxide (0.43 g, 7.64 mmol) were heated at 80 °C using tetrabutylammonium bromide (NBu₄Br) (1.03 g, 3.18 mmol) as a phase transfer catalyst in the absence of solvent. The imidazolium (0.88 g, 3.75 mmol) was subsequently reacted with 2,4-difluorophenylboronic acid (0.88 g, 5.60 mmol), Pd(dppf)Cl₂ (0.11 g, 0.15 mmol), and K₂CO₃ (2.07 g, 15.00 mmol) in a mixture of toluene (15 mL), ethanol (3 mL), and water (3 mL). The reaction mixture was heated at 110 °C for 12 h to form 4-(*t*-butyl)-2-(2,4-difluorophenyl)-6-(1*H*-imidazol-1-yl)pyridine. The isolated product (1.15 g, 3.68 mmol) were then heated with 2-iodopropane (0.8 mL, 8.07 mmol) in toluene (40 mL) to afford 1-[4-(*t*-butyl)-6-(2,4-difluorophenyl)pyridin-2-yl]-3-isopropyl-1*H*-imidazol-3-ium iodide. This imidazolium iodide pre-ligand (1.5 g, 3.1 mmol) was subjected to anion exchange using NH₄PF₆ (4.04 g, 25 mmol), and stirring in ethanol for 2 hours. Addition of water resulted in the precipitation of (phpyim-H₂)PF₆. The overall yield in the multi-stepped synthetic procedures is approx. 61 %.

Spectral data of (phpyim-H₂)PF₆: ¹H NMR (400 MHz, CDCl₃): δ 9.53 (s, 1H), 8.24 (s, 1H), 8.01 ~ 7.95 (m, 1H), 7.88 (s, 1H), 7.81 (s, 1H), 7.48 (s, 1H), 7.06 ~ 7.02 (m, 1H), 6.97 ~ 6.92 (m, 1H), 4.99 ~ 4.96 (m, 1H, CH), 1.59 (d, *J* = 6.6 Hz, 3H, Me), 1.58 (d, *J* = 6.6 Hz, 3H, Me), 1.42 (s, 9H, *t*-Bu). ¹³C NMR (100 MHz, CDCl₃): 166.63, 163.70 (dd, *J*_{CF} = 251.4, 12.2 Hz), 160.70 (dd, *J*_{CF} = 252.2, 11.9 Hz), 152.32 (d, *J*_{CF} = 3.1 Hz), 146.03, 132.57 (dd, *J*_{CF} = 9.9, 4.0 Hz), 132.01, 122.56 (d, *J*_{CF} = 10.9 Hz), 121.83 (dd, *J*_{CF} = 10.9, 3.8 Hz), 120.52, , 120.13, 112.36 (dd, *J*_{CF} = 21.0, 3.6 Hz), 109.73, 104.51 (t, *J*_{CF} = 26.2 Hz), 54,31, 35.79, 30.26, 22.61. ¹⁹F NMR (376 MHz, CDCl₃): δ -70.90 (d, *J* = 712 Hz, PF₆), -107.10 (s, 1F), -111.65 (s, 1F).

Complex 1. Complex **1** was prepared in a consecutive two-step reaction. A mixture of (phpyim-H₂)PF₆ (470 mg, 0.94 mmol), [Ir(COD)(μ-Cl)]₂ (300 mg, 0.45 mmol) and NaOAc (366 mg, 4.47 mmol) was first heated in anhydrous acetonitrile (20 mL)

for 12 hours and then evaporated to dryness. After then, decalin (20 mL) and pyrazole ligand L1 (316 mg, 1.03 mmol) were added and the mixture was subsequently refluxed overnight. For workup, yellow product was obtained by column chromatography eluting with pure CH₂Cl₂ solvent. The overall yield in two-step process: 23 %. Single crystals were obtained from a layered solution of CH₂Cl₂ and hexane at RT.

Spectral data of **1**: ¹H NMR (400 MHz, CDCl₃): δ 8.14 (s, 1H), 7.76 (t, *J* = 8.0 Hz, 1H), 7.60 ~ 7.55 (m, 4H), 7.37 (s, 1H), 6.91 (s, 1H), 6.79 (d, *J* = 2.4 Hz, 1H), 6.56 ~ 6.51 (m, 1H), 6.32 ~ 6.26 (m, 1H), 5.53 (d, *J* = 8.0 Hz, 2H), 3.53 ~ 3.29 (m, 1H, CH), 1.54 (s, 9H, *t*-Bu), 0.80 (d, *J* = 6.8 Hz, 3H, Me), 0.74 (d, *J* = 6.8 Hz, 3H, Me). ¹³C NMR (100 MHz, d₆-acetone): 173.9, 169.8, 165.9, 165.3, 164.5 (dd, *J*_{CF} = 256, 11 Hz), 163.7, 163.4, 163.4, 162.8, 162.7 (dd, *J*_{CF} = 257.7, 11.6 Hz), 153.6, 152.5, 151.2, 142.1, 141.8 (q, *J*_{CF} = 36 Hz), 138.1, 129.6, 127.6 (d, *J*_{CF} = 9.1 Hz), 123.9 (q, *J*_{CF} = 266 Hz), 119.1, 118.4, 117.6 (d, *J*_{CF} = 16.7 Hz), 116.5 (d, *J*_{CF} = 18.0 Hz), 115.2 (d, *J*_{CF} = 11.9 Hz), 113.6 (dd, *J*_{CF} = 14.2, 2.8 Hz), 108.7 (d, *J*_{CF} = 23 Hz), 104.9, 103.3, 98.6 (t, *J*_{CF} = 26.7 Hz), 52.9, 36.7, 27.7, 22.6. ¹⁹F NMR (376 MHz, CDCl₃): δ -59.81 (s, 3F), -107.49 (d, *J* = 9.8 Hz, 1F), -110.48 (d, *J* = 9.8 Hz, 1F), 110.52 (s, 1F). MS [FAB]: *m/z* 852.6, M⁺. Anal. Calcd. for C₃₆H₂₉F₆IrN₆: C, 50.76; H, 3.43; N, 9.87. Found: C, 50.64; H, 3.77; N, 9.48.

Selected crystal data of **1**: C_{36.50}H₃₀ClF₆IrN₆; *M* = 894.32; *T* = 200(2) K; λ(Mo-K_α) = 0.71073 Å; monoclinic; space group = C2/c; *a* = 23.0408(11), *b* = 10.8244(5), *c* = 28.9246(13) Å, β = 95.7113(11)°; *V* = 7178.1(6) Å³; *Z* = 8; ρ_{calcd} = 1.655 Mg·cm⁻³; μ = 3.861 mm⁻¹; *F*(000) = 3512; crystal size = 0.36 × 0.25 × 0.20 mm³; 27270 reflections collected, 8246 independent reflections (*R*_{int} = 0.0475), max. and min. transmission = 0.5123 and 0.3370, restraints / parameters = 56 / 477, GOF = 1.050, final *R*₁ [*I* > 2σ(*I*)] = 0.0378 and *wR*₂(all data) = 0.0985, largest diff. peak and hole = 1.191 and -0.708 e·Å⁻³.

Complex 2. Complex **2** was synthesized using the similar method as described in **1**. (phpyim-H₂)PF₆ (303 mg, 0.63 mmol), [Ir(COD)(μ-Cl)]₂ (200 mg, 0.30 mmol) and NaOAc (244 mg, 2.98 mmol) in CH₃CN solution (20 mL) were refluxed overnight. After

evaporation of solvent, ligand L2 (245 mg, 0.68 mmol) and decalin were added. The mixture was heated at 200°C for one-day and the solvent was removed. The yellow product was obtained after column chromatography eluting with CH₂Cl₂ solution. Yield: 26 %. Complexes **3** – **5** were prepared from L3–L5 using this generalized method with yields of 25, 35 and 27 %, respectively. Single crystals of **5** were obtained from a layered solution of CH₂Cl₂ and heptane at RT.

Spectral data of **2**: ¹H NMR (400 MHz, CDCl₃): δ 8.15 (s, 1H), 7.81 (t, *J* = 8.0 Hz, 1H), 7.72 (d, *J* = 8.0 Hz, 1H), 7.67 (d, *J* = 8.0 Hz, 1H), 7.64 (d, *J* = 8.0 Hz, 1H), 7.58 (s, 1H), 7.39 (s, 1H), 7.05 (d, *J* = 8.0 Hz, 1H), 6.93 (s, 1H), 6.81 (s, 1H), 6.33 ~ 6.27 (m, 1H), 6.05 (s, 1H), 5.49 (s, 1H), 3.33 ~ 3.27 (m, 1H, CH), 1.53 (s, 9H, *t*-Bu), 0.80 (d, *J* = 6.8 Hz, 3H, Me), 0.74 (d, *J* = 6.8 Hz, 3H, Me). ¹³C NMR (100 MHz, d₆-acetone): 173.6, 169.4, 166.2, 164.6 (dd, *J*_{CF} = 256, 11.0 Hz), 163.4, 163.4, 163.2, 162.7 (dd, *J*_{CF} = 258, 11.9 Hz), 154.0, 153.6, 151.0, 149.6 (d, *J*_{CF} = 27.1 Hz), 142.1 (q, *J*_{CF} = 35.6 Hz), 138.3, 130.4, 129.5, 127.6, 125.1 (q, *J*_{CF} = 271 Hz), 123.9 (q, *J*_{CF} = 266 Hz), 119.2, 118.7, 118.6, 118.6, 116.6, 116.3, 116.0 (d, *J*_{CF} = 17.8 Hz), 113.5 (dd, *J*_{CF} = 15.4, 2.8 Hz), 105.0, 103.6, 98.2 (t, *J*_{CF} = 26.7 Hz), 53.0, 36.8, 22.7, 22.5. ¹⁹F NMR (376 MHz, CDCl₃): δ –59.89 (s, 3F), –62.81 (s, 3F), –107.42 (d, *J* = 9.8 Hz, 1F), –110.35 (d, *J* = 9.8 Hz, 1F). MS [FAB]: *m/z* 902.7, M⁺. Anal. Calcd. for C₃₇H₂₉F₈IrN₆: C, 49.27; H, 3.24; N, 9.32. Found: C, 49.29; H, 3.33; N, 8.91.

Spectral data of **3**: ¹H NMR (400 MHz, CDCl₃): δ 8.13 (s, 1H), 7.72 (t, *J* = 8.0 Hz, 1H), 7.59 ~ 7.56 (m, 3H), 7.46 ~ 7.44 (m, 2H), 6.92 (s, 1H), 6.82 (dd, *J* = 8.0 Hz, 2.0 Hz, 1H), 6.73 (d, *J* = 2.0 Hz, 1H), 6.30 ~ 6.24 (m, 1H), 5.64 (d, *J* = 2.0 Hz, 1H), 5.60 (dd, *J* = 8.0 Hz, 2.0 Hz, 1H), 3.39 ~ 3.32 (m, 1H), 1.50 (s, 9H, *t*-Bu), 0.92 (s, 9H, *t*-Bu), 0.81 (d, *J* = 6.8 Hz, 3H, Me), 0.69 (d, *J* = 6.8 Hz, 3H, Me). ¹³C NMR (125 MHz, CD₂Cl₂): 174.7, 169.0, 165.1, 164.2 (dd, *J*_{CF} = 257, 10.6 Hz), 164.1, 163.4, 163.3, 162.3 (dd, *J*_{CF} = 247, 11.5 Hz), 152.9, 151.2, 146.8, 142.0 (q, *J*_{CF} = 34.2 Hz), 141.8, 136.8, 129.8, 129.0, 126.5, 124.6, 123.3 (d, *J*_{CF} = 267 Hz), 118.8, 117.6, 117.0, 116.0 (d, *J*_{CF} = 17.6 Hz), 114.3 (d, *J*_{CF} = 19.6 Hz), 113.4, 113.0, 103.1, 102.6, 97.9 (t, *J*_{CF} = 26.5 Hz), 52.2, 36.2, 34.4, 31.1, 31.0, 30.7, 22.8, 22.6. ¹⁹F NMR (376 MHz, CDCl₃): δ –59.77 (s, 3F), –107.80

(d, $J = 9.8$ Hz, 1F), -111.36 (d, $J = 9.8$ Hz, 1F). MS [FAB]: m/z , 890.7 M^+ . Anal. Calcd. for $C_{40}H_{38}F_5IrN_6$: C, 53.98; H, 4.30; N, 9.44. Found: C, 54.19; H, 4.53; N, 9.05.

Spectral data of **4**: 1H NMR (400 MHz, $CDCl_3$): δ 8.61 (d, $J = 8.0$ Hz, 1H), 8.38 (d, $J = 8.0$ Hz, 1H), 8.17 (s, 1H), 7.82 (t, $J = 8.0$ Hz, 1H), 7.65 ~ 7.60 (m, 2H), 7.56 (d, $J = 2.0$ Hz, 1H), 7.48 (t, $J = 8$ Hz, 1H), 7.41 (s, 1H), 7.28 (t, $J = 8.0$ Hz, 1H), 7.10 (d, $J = 8.0$ Hz, 1H), 6.94 (s, 1H), 6.73 (d, $J = 2.0$ Hz, 1H), 6.28 ~ 6.22 (m, 1H), 6.11 (d, $J = 8.0$ Hz, 1H) 5.45 (d, $J = 8.0$ Hz, 1H), 3.45 ~ 3.39 (m, 1H, CH), 1.55 (s, 9H, *t*-Bu), 0.76 (d, $J = 6.8$ Hz, 3H, Me), 0.73 (d, $J = 6.8$ Hz, 3H, Me). ^{13}C NMR (125 MHz, d_6 -acetone): 173.9, 170.2, 165.7, 165.4, 164.5 (dd, $J_{CF} = 256, 11.1$ Hz), 163.4, 163.4, 162.6 (dd, $J_{CF} = 257, 11.6$ Hz), 156.1, 154.5, 153.5, 151.3, 142.0 (q, $J_{CF} = 34.9$ Hz), 137.8, 137.6, 133.3, 131.7, 131.0, 130.5, 130.3, 129.5, 127.7, 124.6 (q, $J_{CF} = 266$ Hz), 123.2, 122.0, 119.1 (d, $J_{CF} = 27.6$ Hz), 118.5, 115.9 (d, $J_{CF} = 18.1$ Hz), 114.4, 113.6 (d, $J_{CF} = 15.3$ Hz), 104.8, 103.3, 97.6 (t, $J_{CF} = 26.8$ Hz), 52.8, 36.7, 31.1, 22.7, 22.5. ^{19}F NMR (376 MHz, $CDCl_3$): δ -59.75 (s, 3F), -107.24 (d, $J = 9.8$ Hz, 1F), -110.65 (d, $J = 9.8$ Hz, 1F). MS [FAB]: m/z , 884.5 M^+ . Anal. Calcd. for $C_{40}H_{32}F_5IrN_6$: C, 54.35; H, 3.65; N, 9.51. Found: C, 54.17; H, 3.99; N, 9.23.

Spectral data of **5**: 1H NMR (400 MHz, $CDCl_3$): δ 8.95 (d, $J = 8.0$ Hz, 1H), 8.32 (d, $J = 8.0$ Hz, 1H), 8.14 (s, 1H), 8.05 (d, $J = 7.6$ Hz, 1H), 7.98 (s, 1H), 7.73 ~ 7.67 (m, 2H), 7.56 (d, $J = 2.0$ Hz, 1H), 7.39 (s, 1H), 6.94 (s, 1H), 6.93 (t, $J = 6.8$ Hz, 1H), 6.75 (d, $J = 2.0$ Hz, 1H), 6.71 (t, $J = 7.6$ Hz, 1H), 6.28 ~ 6.22 (m, 1H), 6.06 (d, $J = 6.8$ Hz, 1H), 5.45 (m, 1H), 3.34 ~ 3.27 (m, 1H, CH), 1.54 (s, 9H, *t*-Bu), 0.72 (d, $J = 6.8$ Hz, 3H, Me), 0.66 (d, $J = 6.8$ Hz, 3H, Me). ^{19}F NMR (376 MHz, $CDCl_3$): δ -59.65 (s, 3F), -107.69 (d, $J = 9.8$ Hz, 1F), -110.85 (d, $J = 9.8$ Hz, 1F). MS [FAB]: m/z , 884.3 M^+ . $C_{40}H_{32}F_5IrN_6$: C, 54.35; H, 3.65; N, 9.51. Found: C, 54.01; H, 4.03; N, 9.15.

Selected crystal data of **5**: $C_{41.33}H_{34.67}Cl_{2.67}F_5IrN_6$; $M = 997.15$; $T = 150(2)$ K; $\lambda(Mo-K\alpha) = 0.71073$ Å; trigonal; space group = $R\bar{3}c$; $a = b = 43.0841(10)$ and $c = 22.6082(5)$ Å; $V = 36343.8(19)$ Å³; $Z = 36$; $\rho_{calcd} = 1.640$ Mg·cm⁻³; $\mu = 3.544$ mm⁻¹; $F(000) = 17712$; crystal size = $0.25 \times 0.24 \times 0.20$ mm³; 60031 reflections collected, 9278 independent reflections ($R_{int} = 0.0396$), max. and min. transmission = 0.7456

and 0.6350, restraints / parameters = 55 / 563, GOF = 1.052, final $R_1 [I > 2\sigma(I)] = 0.0289$ and wR_2 (all data) = 0.0682, largest diff. peak and hole = 0.685 and $-1.291 \text{ e}\cdot\text{\AA}^{-3}$.

Complex 6. Complex **6** was prepared using identical procedure as described for **5**, except that xylene was used instead of decalin in the second-step. Hence, the red product was obtained after column chromatography eluting with a 1:4 mixture of ethyl acetate and hexane. Yield: 20 %. Single crystals were obtained from a layered solution of CH_2Cl_2 and heptane at RT.

Spectral data of **6**: ^1H NMR (400 MHz, CDCl_3): δ 8.08 (s, 1H), 7.81 (d, $J = 8.2$ Hz, 1H), 7.66 (s, 1H), 7.56 (t, $J = 7.4$ Hz, 1H), 7.34 (s, 1H), 7.17 (t, $J = 7.4$ Hz, 1H), 7.11 (s, 1H), 7.02 ~ 6.98 (m, 2H), 6.92 ~ 6.81 (m, 3H), 6.63 (s, 1H), 6.53 (d, $J = 7.4$ Hz, 1H), 6.33 ~ 6.27 (m, 1H), 6.19 (d, $J = 7.4$ Hz, 2H), 4.01 ~ 3.95 (m, 1H, CH), 1.44 (s, 9H, *t*-Bu), 1.32 (d, $J = 6.8$ Hz, 3H, Me), 0.84 (d, $J = 6.8$ Hz, 3H, Me), -23.47 (s, 1H, M-H). ^{19}F NMR (376 MHz, CDCl_3): δ -59.93 (s, 3F), -108.02 (d, $J = 9.8$ Hz, 1F), -112.82 (d, $J = 9.8$ Hz, 1F). MS [FAB]: m/z , 886.2 M^+ . $\text{C}_{40}\text{H}_{34}\text{F}_5\text{IrN}_6$: C, 54.23; H, 3.87; N, 9.49. Found: C, 53.99; H, 4.12; N, 9.25.

Selected crystal data of **6**: $\text{C}_{82.50}\text{H}_{73}\text{Cl}_5\text{F}_{10}\text{Ir}_2\text{N}_{12}$; $M = 1984.17$; $T = 150(2)$ K; $\lambda(\text{Mo-K}\alpha) = 0.71073$ \AA ; triclinic; space group = P-1; $a = 12.2533(10)$ $b = 12.2839(10)$ and $c = 26.849(2)$ \AA ; $V = 3934.5(5)$ \AA^3 ; $Z = 2$; $\rho_{\text{calcd}} = 1.675$ $\text{Mg}\cdot\text{cm}^{-3}$; $\mu = 3.626$ mm^{-1} ; $F(000) = 1962$; crystal size = $0.31 \times 0.19 \times 0.09$ mm^3 ; 35943 reflections collected, 18047 independent reflections ($R_{\text{int}} = 0.0152$), max. and min. transmission = 0.7456 and 0.5711, restraints / parameters = 26 / 1034, GOF = 1.073, final $R_1 [I > 2\sigma(I)] = 0.0242$ and wR_2 (all data) = 0.0511, largest diff. peak and hole = 1.230 and $-1.239 \text{ e}\cdot\text{\AA}^{-3}$.

Conversion of 6 to 5. A solution of **6** (50 mg, 0.06 mmol) and NaOAc (10 mg, 0.12 mmol) in 5 mL of decalin was refluxed at 200 °C for 18 hours. Removal of solvent and purification by column chromatography eluting with a 1:4 mixture of ethyl acetate and hexane afforded the red complex **5** in 85 % yield.

Single Crystal X-Ray Diffraction Studies: Single crystal X-ray diffraction study

was performed with a Bruker SMART Apex CCD diffractometer using (Mo-K α) radiation ($\lambda = 0.71073 \text{ \AA}$). The data collection was executed using the SMART program. Cell refinement and data reduction were performed with the SAINT program. An empirical absorption was applied based on the symmetry-equivalent reflections and the SADABS program. The structures were solved using the SHELXS-97 program and refined using the SHELXL-97 program by full-matrix least squares on F^2 values. The structural analysis and molecular graphics were obtained using the SHELXTL program on a PC.

Cyclic Voltammetry. The electrochemical properties of these complexes were studied on a CHI621A Electrochemical Analyzer. Platinum wire and Ag/Ag⁺ act as counter electrode and reference electrode, respectively. For the oxidation potential measurements, the glassy carbon electrode was used as the working electrode and 0.1M NBu₄PF₆ in CH₂Cl₂ was used as the supporting electrolyte. For the reduction measurements, the gold electrode and 0.1 M NBu₄PF₆ in THF solution were used, respectively. The potentials were referenced externally to the ferrocenium/ferrocene (FcH⁺/FcH) couple.

Computational Studies. Calculations were performed with the Gaussian 09 program package using the B3LYP functional,²⁶ and LANL2DZ basis set²⁷ for iridium and 6-31G** for all other atoms.²⁸ A conductor-like polarization continuum model CPCM of CH₂Cl₂ solvent was applied to all calculations, and the results were analyzed further with GaussSum.²⁹ Structures obtained were confirmed as true minima by the absence of imaginary frequencies. TD-DFT computations were carried out on the optimized ground state geometries of **1-5** to predict their absorption data. The predicted S₀ ← T₁ emission wavelengths were converted from the TD-DFT absorption wavelengths of S₀ → T₁ using an energy scaling factor³⁰ of 0.94 to take into account the expected constant Stokes shift in these iridium complexes.¹² The model chemistry B3LYP/LANL2DZ:6-31G**/PCM used here has been shown to be appropriate for iridium complexes elsewhere.³¹

OLED Fabrication. Two kinds of ITO-coated glass (i.e., 70 nm and 90 nm) were

purchased from Ruilong. Their sheet resistances were measured to be 50 and 25 Ω /square, respectively. All purchased organic materials were subjected to the high vacuum temperature-gradient sublimation before use. The organic and metal layers were deposited by thermal evaporation in a vacuum chamber with a base pressure of $< 10^{-6}$ Torr. Device fabrication was completed in a single cycle without breaking the vacuum. The OLED architecture consists of multiple organic layers and a reflective cathode consecutively deposited onto the ITO-coated glass substrate. The deposition rates of organic materials and aluminum were respectively kept at around 0.1 nm/s and 0.5 nm/s. The active area was defined by the shadow mask ($2 \times 2 \text{ mm}^2$). Current density-voltage-luminance characterization was measured using a Keithley 238 current source-measure unit and a Keithley 6485 picoammeter equipped with a calibrated Si-photodiode. The electroluminescent spectra were recorded using an Ocean Optics spectrometer.

Supporting information. CIF data of Ir(III) complexes **1**, **5** and **6** and detailed MO data of the Ir(III) complexes **1–5**. Cyclic voltammogram of Ir(III) metal complexes **1–6**, and ^{13}C NMR spectra of (ppyim- H_2)PF₆ and complexes **1–4**.

Acknowledgments. This work was supported by the Ministry of Science and Technology of Taiwan, under the grant numbers 102-2221-E-155-080-MY3. P.J.L. gratefully acknowledges support from the ARC and award of a Future Fellowship (FT120100073). W.-Y.W. acknowledges the financial support from the Areas of Excellence Scheme of the University Grants Committee (AoE/P-03/08), the National Basic Research Program of China (2013CB834702), Hong Kong Research Grants Council (HKBU12304715), Hong Kong Baptist University (FRG1/14-15/084) and Dr. Elizabeth Law for the Endowed Chair Professorship of Advanced Materials.

Notes: The authors declare no competing financial interests.

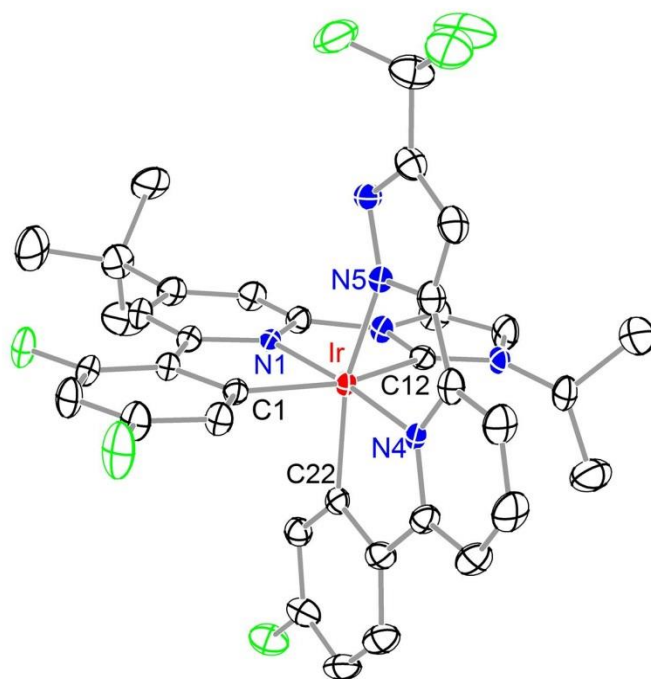


Figure 1. Structural drawing of Ir(III) complex **1** with ellipsoids shown at the 30 % probability, selected bond distances: Ir-C(1) = 2.040(4), Ir-N(1) = 1.990(4), Ir-C(12) = 2.047(5), Ir-N(5) = 2.113(4), Ir-N(4) = 1.995(4) and Ir-C(22) = 2.024(5) Å; selected bond angles: C(1)-Ir-C(12) = 158.18(19), N(5)-Ir-C(22) = 158.79(18) and N(1)-Ir-N(4) = 174.77(15)°.

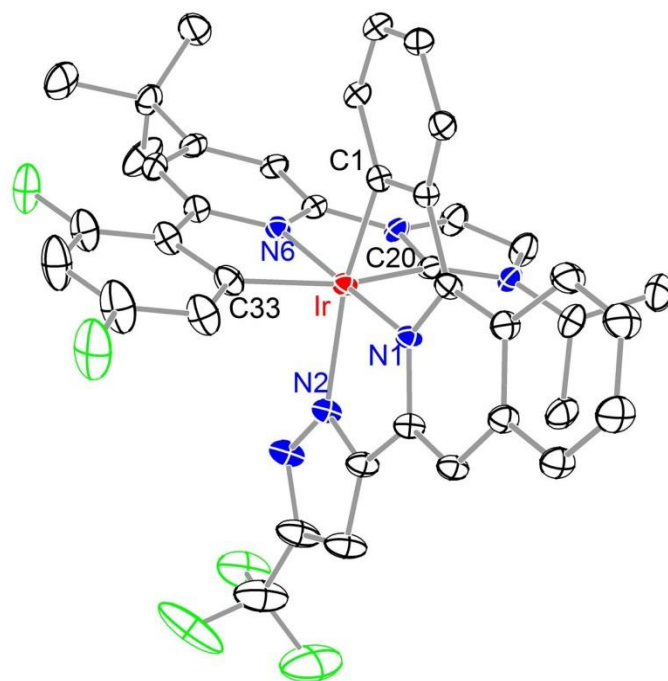


Figure 2. Structural drawing of Ir(III) complex **5** with ellipsoids shown at the 30 % probability, selected bond distances: Ir-C(1) = 2.016(3), Ir-N(1) = 1.999(3), Ir-N(2) = 2.097(3), Ir-C(20) = 2.051(3), Ir-N(6) = 1.996(3), Ir-C(33) = 2.037(4) Å; selected bond angles: C(1)-Ir-N(2) = 159.09(12), C(20)-Ir-C(33) = 158.37(13) and N(1)-Ir-N(6) = 175.27(11)°.

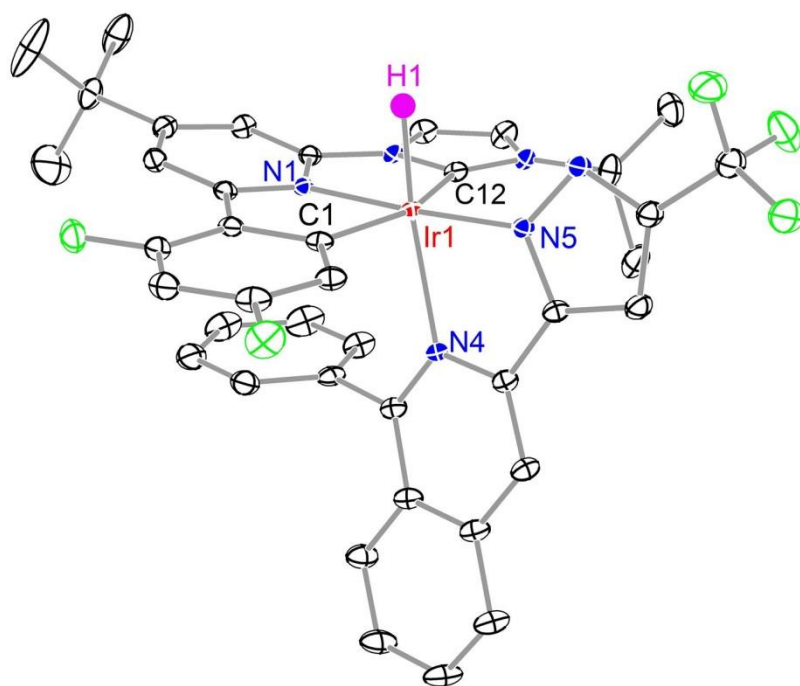


Figure 3. Structural drawing of Ir(III) complex **6** with ellipsoids shown at the 30 % probability, selected bond distances: Ir(1)-C(1) = 2.051(3), Ir(1)-C(12) = 2.027(3), Ir(1)-N(1) = 1.996(2), Ir(1)-N(4) = 2.229(2), Ir(1)-N(5) = 2.017(2), Ir(1)-H(1) = 1.65(3) Å; selected bond angles: C(1)-Ir(1)-C(12) = 158.70(12), N(1)-Ir(1)-N(5) = 176.04(9) and H(1)-Ir(1)-N(4) = 168.4(11)°.

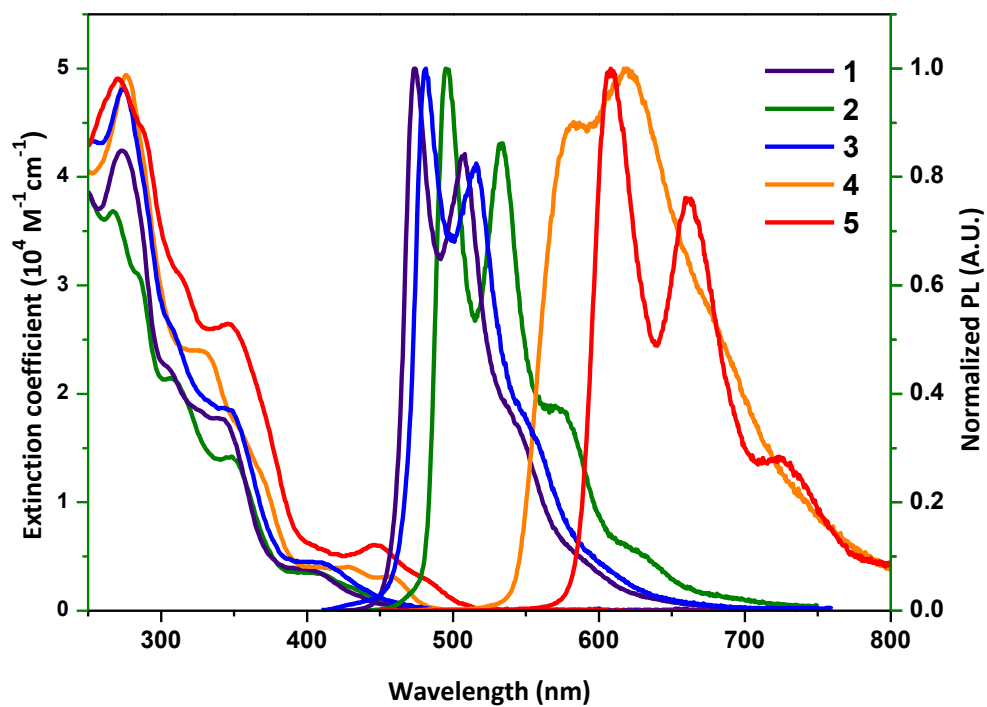


Figure 4. UV/Vis absorption and emission spectra of Ir(III) complexes **1 – 5** in CH₂Cl₂ solution at RT.

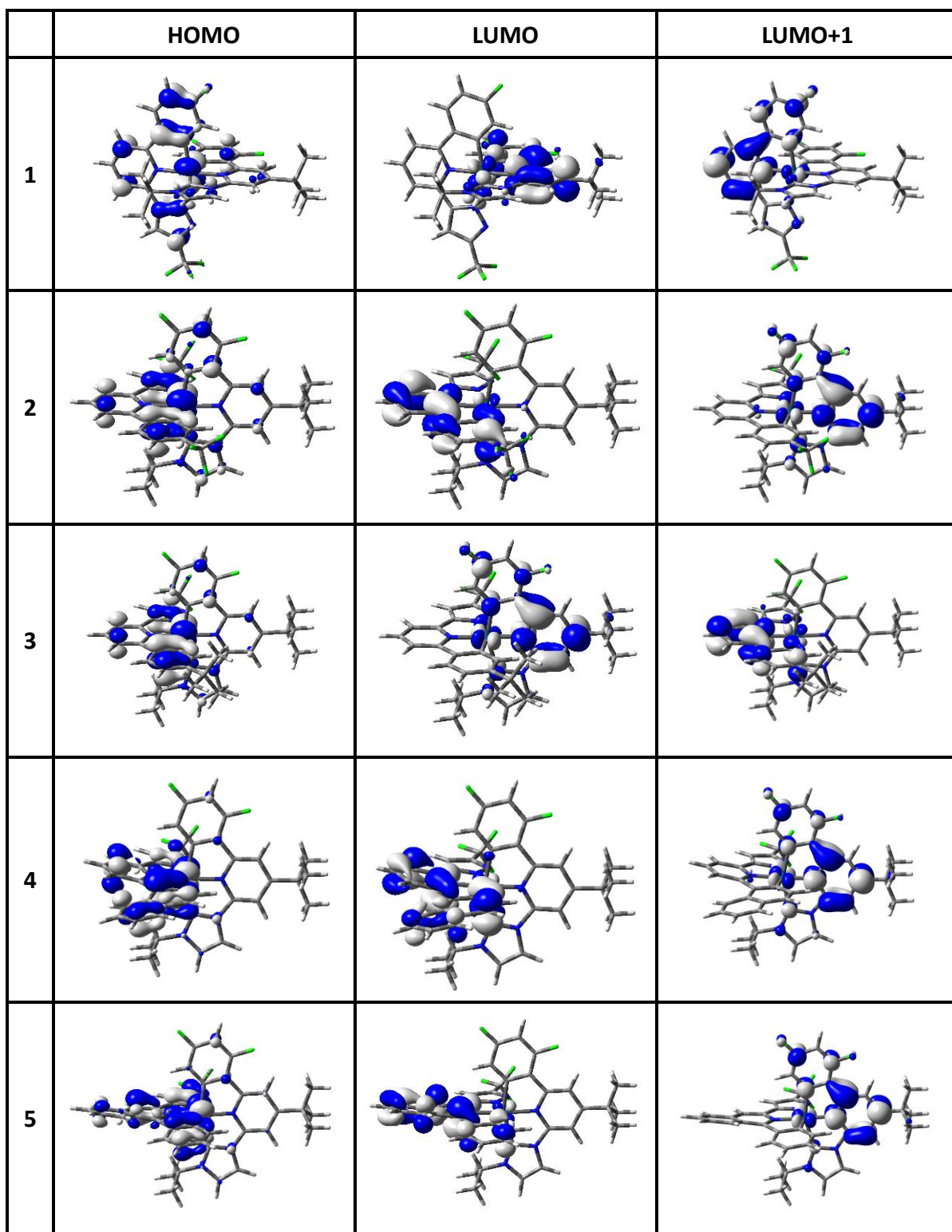


Figure 5. Plots of the HOMO, LUMO and LUMO+1 of the studied Ir(III) complexes. All contours are plotted at ± 0.04 (e/bohr^3)^{1/2}.

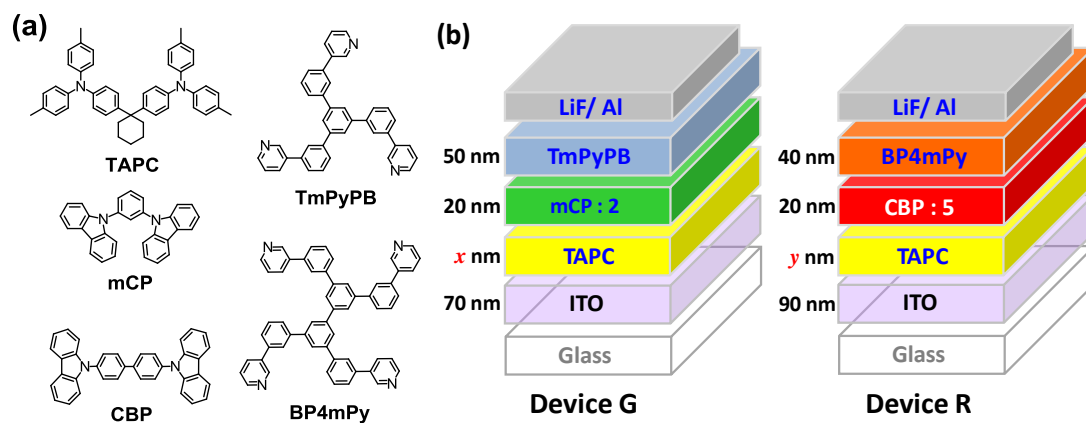


Figure. 6. (a) Molecular structures of the employed materials; (b) schematic architecture of OLED devices with complexes **2** and **5**.

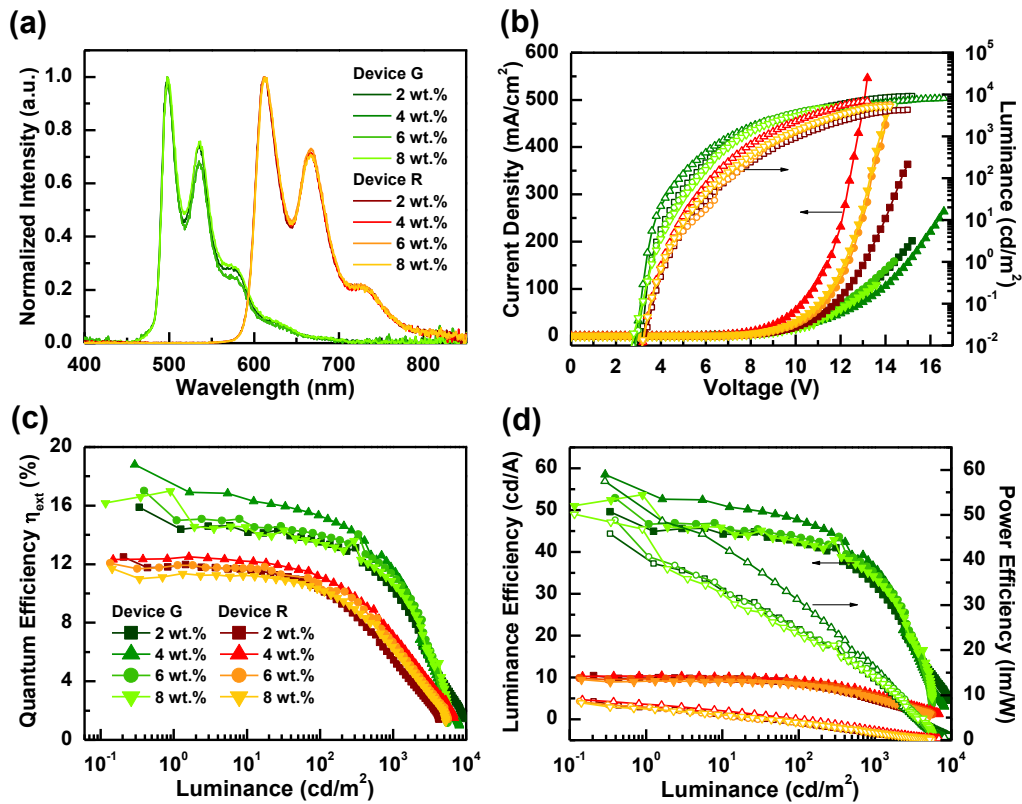


Figure 7. EL characteristics of green and red OLEDs with different doping concentrations. (a) EL spectra; (b) current density-voltage-luminance (J - V - L) curves; (c) external quantum efficiency vs. luminance; (d) luminance efficiency and power efficiency as a function of luminance for devices G and R.

Table 1. Photophysical data of the studied Ir(III) complexes **1 – 5** and TD-DFT studies.

	abs λ_{\max} / nm ($\epsilon \times 10^4 \text{ M}^{-1} \text{ cm}^{-1}$) ^[a]	PL em λ_{\max} ^[b]	Q.Y. % ^[b,c]	calc. em λ_{\max} ^[d]	$\tau_{\text{obs}} / \mu\text{s}$ ^[b]	$k_r (\text{s}^{-1})$	$k_{\text{nr}} (\text{s}^{-1})$
1	304 (2.25), 340 (1.77), 398 (0.38)	473, 508	99	474	3.10	3.2×10^5	–
2	311 (2.1), 350 (1.40), 410 (0.34)	495, 534, 574 (sh)	91	491	3.91	2.3×10^5	2.6×10^4
3	310 (2.53), 343 (1.81), 408 (0.44)	481, 515	~100	479	3.01	3.3×10^5	–
4	330 (2.38), 430 (0.4), 458 (0.31)	583, 618	25	576	9.23	2.7×10^4	8.1×10^4
5	345 (2.64), 448 (0.60), 481 (0.29)	608, 663, 725 (sh)	57	619	5.40	1.1×10^5	7.5×10^4

[a] Measured in CH_2Cl_2 with a concentration of 10^{-5} M at RT.

[b] Emission peak maxima (in nm) measured in degassed CH_2Cl_2 solution at RT.

[c] Coumarin (C153) in EtOH (Q.Y. = 58 % and λ_{\max} = 530 nm) and 4-dicyanomethylene-2-methyl-6-(4-dimethylaminostyryl)-4H-pyran in DMSO (Q.Y. = 80 % and λ_{\max} = 637 nm) were employed as standard.

[d] Emission peak maxima (in nm) predicted from TD-DFT computations.

Table 2. Electrochemical and DFT MO energy data for the studied Ir(III) complexes **1 – 5**.

	$E_{1/2}^{\text{Ox}}$ (V) [ΔE_p] ^[a]	$E_{\text{pc}}^{\text{Re}}$ (V) [ΔE_p] ^[b]	obs HOMO (eV) ^[c]	obs HLG (eV) ^[d]	obs LUMO (eV) ^[e]	calc HOMO (eV) ^[f]	calc HLG (eV) ^[f]	calc LUMO (eV) ^[f]	calc LUMO+1 (eV) ^[f]
1	0.66 [0.06]	-2.58 [irr]	-5.46	3.21	-2.25	-5.43	3.83	-1.60	-1.43
2	0.71 [0.08]	-2.67 [irr]	-5.51	3.34	-2.17	-5.49	3.81	-1.68	-1.62
3	0.57 [0.07]	-2.62 [irr]	-5.37	3.16	-2.21	-5.34	3.77	-1.57	-1.40
4	0.54 [0.07]	-2.61 [irr]	-5.34	3.12	-2.22	-5.25	3.61	-1.64	-1.60
5	0.57 [0.09]	-2.40 [irr]	-5.37	2.92	-2.45	-5.29	3.36	-1.93	-1.61

[a] $E_{1/2}$ (mV) refers to $[(E_{\text{pa}} + E_{\text{pc}})/2]$, where E_{pa} and E_{pc} are the anodic and cathodic potential peak referenced to the ferrocene ($\text{FcH}/\text{FcH}^+ = -4.8$ eV) in CH_2Cl_2 solution at RT.³²

[b] E_{pc} is the cathodic peak potential and “irr” denotes an irreversible process. Reduction potential was measured in degassed THF at RT.

[c] $\text{HOMO} = -4.8 - E_{1/2}^{\text{Ox}}$.

[d] HOMO-LUMO gap (HLG) = energy difference calculated from two anodic waves, $E_{\text{pa}}^{\text{Ox}} - E_{\text{pa}}^{\text{Re}}$.

[e] $\text{LUMO} = \text{HOMO} + \text{HLG}$

[f] Values from electronic structure DFT calculations; LUMO+1 energy data included as LUMO and LUMO+1 are close in energy.

Table 3. EL characteristics of tested devices with different doping concentrations.

Device		Green				Red			
		mCP/ 2				CBP/ 5			
Host/ dopant									
HTL/ ETL		TAPC (70 nm)/ TmPyPB (50 nm)				TAPC (40 nm)/ BP4mPy (40 nm)			
conc. (wt.%)		2	4	6	8	2	4	6	8
<i>EQE (%)</i>	[a]	15.9	18.8	17.0	17.0	12.5	12.5	12.1	11.7
	[b]	13.5	15.3	14.0	13.5	10.3	11.1	10.5	10.3
<i>LE (cd/A)</i>	[a]	49.6	58.5	52.9	53.7	10.4	10.4	9.8	9.5
	[b]	42.3	47.6	43.6	42.5	8.5	9.3	8.5	8.3
<i>PE (lm/W)</i>	[a]	45.8	57.4	48.9	50.2	8.6	9.0	8.6	8.3
	[b]	24.7	31.0	24.7	23.5	3.8	4.7	3.8	3.9
<i>V_{on} (V)</i>	[c]	3.5	3.3	3.6	3.6	4.3	4.0	4.1	4.1
<i>max. L (cd/m²)</i>		9098	8093	5608	5595	4244	6886	5637	5230
	[voltage]	[15.2]	[16.6]	[14.4]	[13.6]	[15.0]	[13.2]	[14.2]	[14.2]
<i>CIE1931 coordinates</i>	[b]	0.28, 0.60	0.27, 0.60	0.27, 0.60	0.28, 0.60	0.67, 0.33	0.67, 0.33	0.67, 0.33	0.67, 0.32
	[d]	0.28, 0.60	0.27, 0.60	0.27, 0.60	0.28, 0.60	0.67, 0.33	0.67, 0.33	0.67, 0.33	0.67, 0.32

[a] Maximum efficiency; [b] recorded at 10^2 cd/m²; [c] turn-on voltage measured at 1 cd/m²; [d] measured at 10^3 cd/m².

References

- (1) Tang, C. W.; VanSlyke, S. A. *Appl. Phys. Lett.* **1987**, *51*, 913.
- (2) Baldo, M. A.; O'Brien, D. F.; You, Y.; Shoustikov, A.; Sibley, S.; Thompson, M. E.; Forrest, S. R. *Nature* **1998**, *395*, 151.
- (3) (a) You, Y.; Park, S. Y. *Dalton Trans.* **2009**, 1267. (b) Chi, Y.; Chou, P.-T. *Chem. Soc. Rev.* **2010**, *39*, 638-655. (c) Zhou, G.; Wong, W.-Y.; Yang, X. *Chem. Asian J.* **2011**, *6*, 1706-1727.
- (4) (a) Chi, Y.; Chou, P.-T. *Chem. Soc. Rev.* **2007**, *36*, 1421-1431. (b) Chou, P.-T.; Chi, Y. *Chem. Eur. J.* **2007**, *13*, 380-395. (c) Chi, Y.; Tong, B.; Chou, P.-T. *Coord. Chem. Rev.* **2014**, *281*, 1-25.
- (5) (a) Wilkinson, A. J.; Puschmann, H.; Howard, J. A. K.; Foster, C. E.; Williams, J. A. G. *Inorg. Chem.* **2006**, *45*, 8685-8699. (b) Yutaka, T.; Obara, S.; Ogawa, S.; Nozaki, K.; Ikeda, N.; Ohno, T.; Ishii, Y.; Sakai, K.; Haga, M. *Inorg. Chem.* **2005**, *44*, 4737-4746. (c) Obara, S.; Itabashi, M.; Okuda, F.; Tamaki, S.; Tanabe, Y.; Ishii, Y.; Nozaki, K.; Haga, M. *Inorg. Chem.* **2006**, *45*, 8907-8921. (d) Yang, L.; Okuda, F.; Kobayashi, K.; Nozaki, K.; Tanabe, Y.; Ishii, Y.; Haga, M. *Inorg. Chem.* **2008**, *47*, 7154-7165. (e) Ashizawa, M.; Yang, L.; Kobayashi, K.; Sato, H.; Yamagishi, A.; Okuda, F.; Harada, T.; Kuroda, R.; Haga, M. *Dalton Trans.* **2009**, 1700-1702. (f) Kuwabara, J.; Namekawa, T.; Haga, M.; Kanbara, T. *Dalton Trans.* **2012**, *41*, 44-46.
- (6) Williams, J. A. G.; Wilkinson, A. J.; Whittle, V. L. *Dalton Trans.* **2008**, 2081-2099.
- (7) Chen, J.-L.; Wu, Y.-H.; He, L.-H.; Wen, H.-R.; Liao, J.; Hong, R. *Organometallics* **2010**, *29*, 2882-2891.
- (8) (a) Tong, B.; Ku, H. Y.; Chen, I. J.; Chi, Y.; Kao, H.-C.; Yeh, C.-C.; Chang, C.-H.; Liu, S.-H.; Lee, G.-H.; Chou, P.-T. *J. Mater. Chem. C* **2015**, *3*, 3460-3471. (b) Kuei, C.-Y.; Tsai, W.-L.; Tong, B.; Jiao, M.; Lee, W.-K.; Chi, Y.; Wu, C.-C.; Liu, S.-H.; Lee, G.-H.; Chou, P.-T. *Adv. Mater.* **2016**, *28*, 2795-2800.
- (9) (a) Whittle, V. L.; Williams, J. A. G. *Dalton Trans.* **2009**, 3929-3940. (b) Yang, W.-W.; Zhong, Y.-W.; Yoshikawa, S.; Shao, J.-Y.; Masaoka, S.; Sakai, K.; Yao, J.; Haga, M. *Inorg. Chem.* **2011**, *51*, 890-899. (c) Darmawan, N.; Yang, C.-H.; Mauro, M.; Raynal, M.; Heun, S.; Pan, J.; Buchholz, H.; Braunstein, P.; De Cola, L. *Inorg. Chem.* **2013**, *52*, 10756-10765.
- (10) (a) Wu, K.-L.; Li, C.-H.; Chi, Y.; Clifford, J. N.; Cabau, L.; Palomares, E.; Cheng, Y.-M.; Pan, H.-A.; Chou, P.-T. *J. Am. Chem. Soc.* **2012**, *134*, 7488-7496. (b) Chou, C.-C.; Chen, P.-H.; Hu, F.-C.; Chi, Y.; Ho, S.-T.; Kai, J.-J.; Liu, S.-H.; Chou, P.-T. *J. Mater. Chem. A* **2014**, *2*, 5418-5426. (c) Liao, J.-L.; Chi, Y.; Su, Y.-D.; Huang, H.-X.; Chang, C.-H.; Liu, S.-H.; Lee, G.-H.; Chou, P.-T. *J. Mater. Chem. C* **2014**, *2*, 6269-6282.
- (11) (a) Raynal, M.; Pattacini, R.; Cazin, C. S. J.; Vallée, C.; Olivier-Bourbigou, H.; Braunstein, P. *Organometallics* **2009**, *28*, 4028-4047. (b) Chianese, A. R.; Shaner, S. E.; Tendler, J. A.; Pudalov, D. M.; Shopov, D. Y.; Kim, D.; Rogers, S. L.; Mo, A. *Organometallics* **2012**, *31*, 7359-7367.
- (12) Tavasli, M.; Moore, T. N.; Zheng, Y.; Bryce, M. R.; Fox, M. A.; Griffiths, G. C.; Jankus, V.; Al-Attar, H. A.; Monkman, A. P. *J. Mater. Chem.* **2012**, *22*, 6419-6428.
- (13) (a) Koene, B. E.; Loy, D. E.; Thompson, M. E. *Chem. Mater.* **1998**, *10*, 2235. (b) Adachi, C.; Kwong, R.; Forrest, S. R. *Org. Electron.* **2001**, *2*, 37. (c) Holmes, R. J.; Forrest, S. R.; Tung, Y.-J.; Kwong, R. C.; Brown, J. J.; Garon, S.; Thompson, M. E. *Appl. Phys. Lett.* **2003**, *82*, 2422. (d) Su, S.-J.; Sasabe, H.; Takeda, T.; Kido, J. *Chem. Mater.* **2008**, *20*, 1691. (e) Son, K. S.; Yahiro, M.; Imai, T.; Yoshizaki, H.; Adachi, C. *Chem. Mater.* **2008**, *20*, 4439. (f) Tsuboi, T.; Liu, S.-W.; Wu, M.-F.; Chen, C.-T. *Org. Electron.* **2009**, *10*, 1372. (g) Yamada, T.; Suzuki, F.; Goto, A.; Sato, T.; Tanaka, K.; Kaji, H. *Org. Electron.* **2011**, *12*, 169-178. (h) Cai, C.; Su, S.-J.; Chiba, T.; Sasabe, H.; Pu, Y.-J.; Nakayama, K.; Kido, J. *Org. Electron.* **2011**, *12*, 843-850. (i) Volz, D.; Zink, D. M.; Bocksrocker, T.; Friedrichs, J.; Nieger, M.; Baumann, T.; Lemmer, U.; Bräse, S. *Chem. Mater.* **2013**, *25*, 3414-3426.
- (14) (a) Goushi, K.; Kwong, R.; Brown, J. J.; Sasabe, H.; Adachi, C. *J. Appl. Phys.* **2004**, *95*, 7798. (b) Chopra, N.; Lee, J.; Zheng, Y.; Eom, S.-H.; Xue, J.; So, F. *Appl. Phys. Lett.*

- 2008**, 93, 143307. (c) Su, S.-J.; Chiba, T.; Takeda, T.; Kido, J. *Adv. Mater.* **2008**, 20, 2125. (d) Su, S.-J.; Takahashi, Y.; Chiba, T.; Takeda, T.; Kido, J. *Adv. Funct. Mater.* **2009**, 19, 1260.
- (15) (a) Su, S.-J.; Tanaka, D.; Li, Y.-J.; Sasabe, H.; Takeda, T.; Kido, J. *Org. Lett.* **2008**, 10, 941-944. (b) Lin, C.-H.; Hsu, C.-W.; Liao, J.-L.; Cheng, Y.-M.; Chi, Y.; Lin, T.-Y.; Chung, M.-W.; Chou, P.-T.; Lee, G.-H.; Chang, C.-H.; Shih, C.-Y.; Ho, C.-L. *J. Mater. Chem.* **2012**, 22, 10684-10694. (c) Curiel, D.; Mas-Montoya, M.; Chang, C.-H.; Chen, P.-Y.; Tai, C.-W.; Tarraga, A. *J. Mater. Chem. C* **2013**, 1, 3421-3429. (d) Chang, C.-H.; Griniene, R.; Su, Y.-D.; Yeh, C.-C.; Kao, H.-C.; Grazulevicius, J. V.; Volyniuk, D.; Grigalevicius, S. *Dyes Pigm.* **2015**, 122, 257-263.
- (16) (a) Park, Y.-S.; Lee, S.; Kim, K.-H.; Kim, S.-Y.; Lee, J.-H.; Kim, J.-J. *Adv. Funct. Mater.* **2013**, 23, 4914-4920. (b) Huang, Y.-H.; Tsai, W.-L.; Lee, W.-K.; Jiao, M.; Lu, C.-Y.; Lin, C.-Y.; Chen, C.-Y.; Wu, C.-C. *Adv. Mater.* **2015**, 27, 929-934.
- (17) Chang, C.-H.; Ho, C.-L.; Chang, Y.-S.; Lien, I.-C.; Lin, C.-H.; Yang, Y.-W.; Liao, J.-L.; Chi, Y. *J. Mater. Chem. C* **2013**, 1, 2639-2647.
- (18) Chang, C.-H.; Chen, C.-C.; Wu, C.-C.; Yang, C.-H.; Chi, Y. *Org. Electron.* **2009**, 10, 1364.
- (19) Lin, C.-L.; Lin, H.-W.; Wu, C.-C. *Appl. Phys. Lett.* **2005**, 87, 021101.
- (20) Chang, C.-H.; Lin, Y.-H.; Chen, C.-C.; Chang, C.-K.; Wu, C.-C.; Chen, L.-S.; Wu, W.-W.; Chi, Y. *Org. Electron.* **2009**, 10, 1235-1240.
- (21) (a) Holmes, R. J.; D'Andrade, B. W.; Forrest, S. R.; Ren, X.; Li, J.; Thompson, M. E. *Appl. Phys. Lett.* **2003**, 83, 3818. (b) Darmawan, N.; Yang, C.-H.; Mauro, M.; Frohlich, R.; De Cola, L.; Chang, C.-H.; Wu, Z.-J.; Tai, C.-W. *J. Mater. Chem. C* **2014**, 2, 2569-2582.
- (22) Kawamura, Y.; Sasabe, H.; Adachi, C. *Jpn. J. App. Phys.* **2004**, 43, 7729.
- (23) Fu, R.; Bercaw, J. E.; Labinger, J. A. *Organometallics* **2011**, 30, 6751-6765.
- (24) (a) Chung, M.-W.; Lin, T.-Y.; Hsieh, C.-C.; Tang, K.-C.; Fu, H.; Chou, P.-T.; Yang, S.-H.; Chi, Y. *J. Phys. Chem. A* **2010**, 114, 7886. (b) Chi, Y.; Wu, K.-L.; Wei, T.-C. *Chem. Asian J.* **2015**, 10, 1098-1115.
- (25) Chou, P.-T.; Yu, W.-S.; Cheng, Y.-M.; Pu, S.-C.; Yu, Y.-C.; Lin, Y.-C.; Huang, C.-H.; Chen, C.-T. *J. Phys. Chem. A* **2004**, 108, 6487-6498.
- (26) (a) Becke, A. D. *J. Chem. Phys.* **1993**, 98, 5648-5652. (b) Stephens, P. J.; Devlin, F. J.; Chabalowski, C. F.; Frisch, M. J. *J. Phys. Chem.* **1994**, 98, 11623-11627.
- (27) Hay, P. J.; Wadt, W. R. *J. Chem. Phys.* **1985**, 82, 299.
- (28) Petersson, G. A.; Al-Laham, M. A. *J. Chem. Phys.* **1991**, 94, 6081.
- (29) O'Boyle, N. M.; Tenderholt, A. L.; Langner, K. M. *J. Comp. Chem.* **2008**, 29, 839-845.
- (30) (a) Zhang, X.-H.; Wang, L.-Y.; Zhai, G.-H.; Wen, Z.-Y.; Zhang, Z.-X. *J. Mol. Struct. THEOCHEM* **2009**, 906, 50-55. (b) De, A. K.; Ganguly, T. *Spectrochim. Acta A* **2011**, 78, 624-628.
- (31) Liao, J.-L.; Chi, Y.; Sie, Z.-T.; Ku, C.-H.; Chang, C.-H.; Fox, M. A.; Low, P. J.; Tseng, M.-R.; Lee, G.-H. *Inorg. Chem.* **2015**, 54, 10811-10821.
- (32) D'Andrade, B. W.; Datta, S.; Forrest, S. R.; Djurovich, P.; Polikarpov, E.; Thompson, M. E. *Org. Electron.* **2005**, 6, 11-20.